Available online at www.sciencedirect.com

SciVerse ScienceDirect

Acta Materialia 61 (2013) 5561–5570

Acta MATERIALIA

www.elsevier.com/locate/actamat

Effect of Ag–Au composition and acid concentration on dealloying front velocity and cracking during nanoporous gold formation

Yu-chen Karen Chen-Wiegart [a,*], Steve Wang [b], Ian McNulty [c], David C. Dunand [a]

[a] Department of Materials Science and Engineering, Northwestern University, Evanston, IL 60208, USA
[b] Advanced Photon Source, Argonne National Laboratory, Argonne, IL 60439, USA
[c] Center for Nanoscale Materials, Argonne National Laboratory, Argonne, IL 60439, USA

Received 5 December 2012; received in revised form 23 May 2013; accepted 26 May 2013
Available online 12 July 2013

Abstract

Nanoporous gold has many potential applications in various fields, including energy storage, catalysis, sensing and actuating. Dealloying of Ag–Au alloys under free corrosion conditions is a simple method to fabricate nanoporous gold. Here, we systematically investigate the dealloying rate of Ag–*x*Au alloy for a range of alloy compositions ($x = 20$–40 at.%) and nitric acid concentration (7.3–14.9 M) using *in situ* transmission X-ray microscopy. High-resolution *in situ* X-ray projections and *ex situ* tomographic reconstructions allow imaging of the dealloying front position during dealloying. The dealloying front velocity is constant with time, and depends exponentially on the alloy Ag/Au atomic ratio and the acid molar concentration. Only the leanest alloy, Ag–20 Au, shows a large macroscopic shrinkage in sample diameter (~38%) after dealloying, which leads to crack nucleation and growth observed in real time during dealloying. Finite element modeling is used to estimate dealloying-induced stresses and strains, and sheds light on the cracks created by the diameter shrinkage.

Keywords: Nanofoam; TXM; X-ray imaging; In situ

1. Introduction

Dealloying is a simple process used to fabricate various nanoporous metals (Au, Ag, Fe, Co, Ni, Pd, Pt and Ti) [1–8], which have numerous potential applications as functional materials [9,10]. Among all the nanoporous metals, nanoporous gold (np-Au) has the most potential applications including sensors [11], actuators [12], super-capacitors [13], catalytic substrates [14,15], enhanced Raman scattering [16] and anode substrate for Li-ion batteries [17]. The dealloying process for most nanoporous metals involves the use of acid to selectively dissolve the less noble element from a binary alloy, ideally a solid solution, under free corrosion or applied voltage [9]. For np-Au, one of the simplest and most used fabrication method is by free-corrosion dealloying of Ag–Au alloys in concentrated nitric acid, removing the silver atoms while gold atoms self-rearrange into the porous structure, with a typical pore size of 5–20 nm [18].

Dealloying of Ag–Au which results in np-Au can be viewed as a competition between two processes: (i) the dissolution of Ag which results in surface roughening and pore formation and (ii) surface diffusion of Au which results in surface smoothening and passivation [19]. It has been found that the initial length scale of porosity evolution scales inversely with the dealloying front velocity (current density or atomic flux) [20]. This implies that faster

* Corresponding author. Current address: National Synchrotron Light Source, Brookhaven National Laboratory, Upton, NY 11973, USA. Tel.: +1 631 344 3563; fax: +1 631 344 3238.
E-mail addresses: yuchen.karen.chen@gmail.com, ycchen@bnl.gov, yuchenchen@u.northwestern.edu (Y.-c.K. Chen-Wiegart).

1359-6454/$36.00
http://dx.doi.org/10.1016/j.actamat.2013.05.039

dealloying rates will result in smaller pore sizes and thus larger specific areas, which are beneficial for some applications.

Alloy composition and nitric acid concentration, because they alter the chemical potential difference across the nanoporous/alloy interface, are two important parameters that affect the dealloying of Ag–Au alloy in terms of dealloying front velocity and therefore pore size and specific area.

So far, studies of dealloying behavior among various Ag–xAu compositions ($x = x$ at%) mainly emphasize the critical potential (E_c) [19], above which the dealloying process can be sustained and forms a continuous, growing porous layer, and below which the surface becomes passivated and no nanoporosity develops. Dursan et al. have used the "steady-state current" method to determine E_c in Ag–Au with different gold content (20, 25, 30 at.% Au) and showed that once the potential is higher than E_c, the dealloying process proceeds with a potential-dependent steady-state current [24]. In this case, the current density does not vary with alloying time, which is related to the phenomena we report in this paper.

It has been shown in other studies that dealloying of binary alloys only happens when the composition of the more noble metal is below a threshold, or the less noble, more reactive metal is above a threshold, the so-called parting limit [21]. In Ag–Au alloys, the highest Au concentration for which dealloying can take place was reported experimentally to be ~40–45 at.% [22,23]. Conversely, the lower bound composition limit of the more noble metal was also mentioned in the literature. When the atomic percentage of the more noble metal is below the site percolation, termed "dealloying threshold" in the literature, the porous structure does not form [23]. Dursun et al. reported that in the dealloying of Ag–20 Au, the current density could not reach a steady-state because the Au composition is at the site percolation threshold for the face-centered cubic structure [24]. The range 20–40 at.% of Au can therefore be considered to be the window where continuous nanopore formation is possible.

To our knowledge, there has not been a systematic study of the effect of acid concentration on the dealloying kinetics of Ag–Au alloys under a free-corrosion environment. Qian and Chen have studied the temperature effects on pore size evolution during free corrosion of Ag–35 Au for a given acid concentration [25]. They concluded that the pore size evolution, mainly via coarsening in the dealloyed region, was controlled by gold surface diffusion. Other quantitative studies of dealloying consider the effects of applied voltage. For instance, Sieradzki et al. presented a systematic study and modeling on the impact of alloy composition and electrolyte composition upon E_c [19]. They derived a detailed analytical solution on the time evolution of the morphology as a function of E_c, which depends on alloy and electrolyte (acid) composition. Erlebacher et al. simulated the dealloying of Ag–Au using dynamic Monte Carlo simulation with 2–40 at.% of Au under a range of applied voltage [20,26]. In particular, they observed a potential-dependent steady-state current density, which is equivalent to a constant dealloying front velocity. Recently, using *in situ* transmission X-ray microscopy, we found that the dealloying front velocity is constant as a function of the depth of the nano-porous layer (up to 4 μm) for Ag–30 Au alloy dealloyed with 75% (10.9 M) nitric acid [27]. Here, we use this imaging method to systematically investigate the dealloying front velocity for a wide range of alloy compositions and nitric acid concentrations. Also, we investigate dealloying-induced strain and observe crack formation in the alloy with low Au content (20 at.%), whose stress state during the dealloying is modeled numerically.

2. Experimental procedures

2.1. Alloy and acid preparation

Ag–x Au alloys with five different compositions ($x = 20$, 25, 30, 35 and 40 at.%) were prepared by arc melting of the pure elements (99.99% pure, from Kurt J. Lesker) in Ar and labeled Ag–20 Au, Ag–25 Au, Ag–30 Au, Ag–35 Au and Ag–40 Au. Ag–Au alloy wires with various compositions listed above, and diameters of 20–50 μm, were fabricated by remelting the ingot in a Pyrex glass tube under vacuum, which was then drawn into a thin wire (according to the Taylor-wire method [28]), leading to rapid, directional solidification of the alloy. Fracturing the Pyrex exposed the alloy wire, which was shaped into a cylinder (50 μm tall and 16 ± 1 μm in diameter) using focused ion beam milling.

Nitric acid solutions with five different concentrations were prepared by mixing fresh commercial nitric acid with an assay of 68–70 wt.% and deionized water, using 50, 62.5, 75, 87.5 and 100 vol.% of the acid. This resulted in nitric acid concentrations of 7.3, 9.1, 10.9, 12.7 and 14.6 M, respectively.

2.2. X-ray imaging

The transmission X-ray microscope (TXM) [29], located at the beamline 32-ID-C of the Advanced Photon Source (Argonne National Laboratory, IL), was used to measure dealloying distance as a function of time by imaging the dealloying front in Ag–Au wires. TXM is a full-field lens-based imaging technique [29]. A Fresnel zone plate with a 40 nm outmost zone was used as the objective lens, providing 30–40 nm resolution for a two-dimensional (2-D) projection [30]. All images were taken at an X-ray energy of 10.4 keV for an exposure time of 2 s, with a 0.5–3 s delay due to the CCD readout time between exposures. A lens-coupled scintillator and CCD detector were used to record 32.8×32.8 μm images (2048×2048 pixels).

Two sets of experiments were conducted at ambient temperature (~20 °C). First, a fixed nitric acid concentration was used (75 vol.%, as used in our previous study [27]) to dealloy four different Ag–x Au cylinders with four

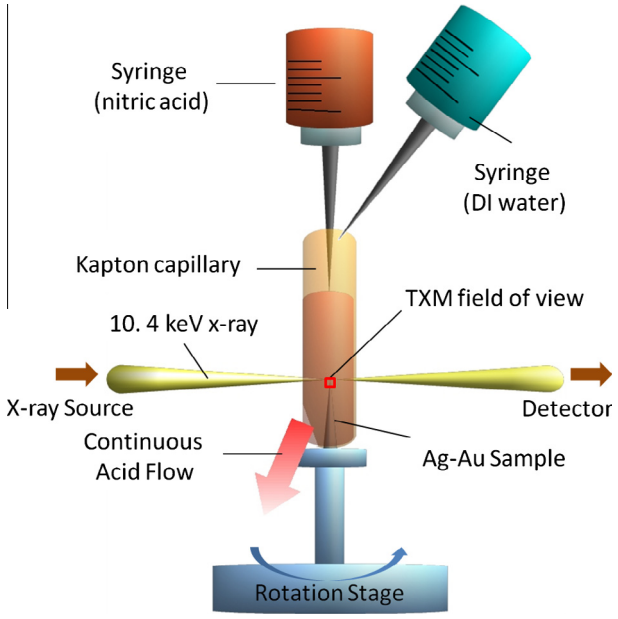

Fig. 1. Schematic of the *in situ* dealloying experimental setup in the transmission X-ray Microscope.

different alloy compositions ($x = 20$, 25, 35 and 40 at.%). Second, four Ag–Au cylinders with a constant Ag–30 Au composition were dealloyed using four nitric acid concentrations: 50, 62.5, 87.5 and 100 vol.% (7.3–14.6 M). Dealloying of Ag–Au with 75 vol.% nitric acid (10.9 M) was reported in our previous work and is included here for comparison [27].

In situ imaging of the dealloying front was carried out by using a custom-design dealloying cell. This allows X-ray imaging under conditions of flowing nitric acid through a Kapton capillary which contains the Ag–Au alloy sample. Two syringes were located on top of the capillary; one contained nitric acid to sustain the dealloying process and the other contained deionized water to terminate the dealloying reaction, so the sample could be imaged in three dimensions by tomographic methods, if necessary. A schematic of the design is shown in Fig. 1. *In situ* imaging was carried out by taking images with 2 s exposure time continuously. The center of the field of view is located at the middle of the cylindrical samples, ~35 μm away from the tip of the cylinder. If some features appeared within the samples (e.g. cracks) which were to be studied in three dimensions, the dealloying process was stopped by injecting deionized water to enable the longer tomographic imaging. Tomography data of the Ag–20 Au sample were collected before dealloying and after full dealloying with 75% nitric acid. The angular step size was 0.5° for a full 180° range with 2 s exposure time. The projections were reconstructed into three-dimensional structure using a standard Filtered Back-projections algorithm [31].

2.3. Finite element modeling

Finite element modeling (FEM) was used to simulate the dealloying-induced stresses and strains due to the diameter shrinkage during dissolution of the silver. The commercial ABAQUS software was used to generate the mesh and calculate the stress and strain distribution.

The Ag–25 Au system was chosen because it developed a volume reduction which could be measured macroscopically using the TXM images. But unlike in the Ag–20 Au system, no cracks were observed during the dealloying of Ag–25 Au so that a simple elasto-plastic behavior could be assumed. For the Ag–20 Au system, FEM would be complicated by the issue of crack nucleation and propagation, while for Ag–30-40 Au, no shrinkage was measured, making FEM superfluous. Fig. 2a shows the shape of the Ag–Au/np-Au cylinder in three dimensions, which was represented by a 2-D model in FEM, using axisymmetric conditions, as shown in Fig. 2b. Half of the cross-section along the vertical direction was divided into Ag–Au and np-Au regions and used for FEM. Due to the cylindrical symmetry of the cylindrical sample, this 2-D model with axissymmetric condition gives an excellent representation of the stresses and strains in a three-dimensional (3-D) cylinder. The axis of symmetry is labeled in Fig. 2a and b as a dashed line [32]. The bottom of the model is fully pinned to simulate that the sample is mechanically clamped by the sample holder.

The type of element chosen was CAX4R – a four-node bilinear axisymmetric quadrilateral, reduced integration, hourglass control. The element size is ~200 nm given the radius (R) and length (L) detailed in the following. As

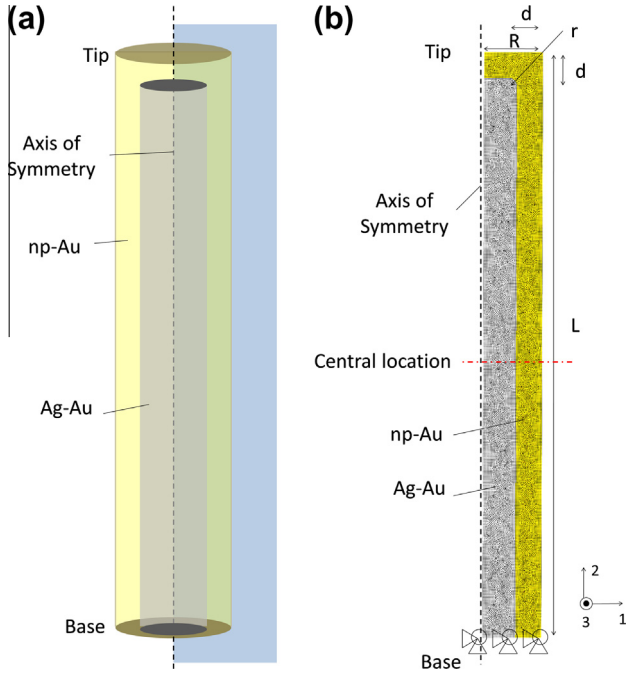

Fig. 2. (a) A 3-D representation of a partially dealloyed cylinder. The blue plane indicates half the of cross-section along the vertical direction, which was used for finite element modeling (FEM). (b) The 2-D model with axissymmetric condition used for FEM. (For interpretation of the references to colour in this figure legend, the reader is referred to the web version of this article.)

shown in Fig. 2b, d is the distance between the dealloying front and the surface of the sample, if no volume shrinkage appears, which increases with the dealloying time and can be measured from TXM images. Although the dealloying front propagates faster near the cylinder top as shown in our previous work [27], a constant d at a given dealloying time was used in the model for simplicity. R is the distance between the surface of the sample and its center, 8.17 μm. L is chosen as $10R$ (81.7 μm) such that the end effects do not affect the stress and strain states in the center of the sample (marked as a red dashed line in Fig. 2). The top-right corner of the interface between np-Au and Ag–Au was rounded with a tangent circle (radius = 1 μm) to simulate the morphology observed in TXM images.

The diameter shrinkage associated with dealloying was modeled as a uniform volumetric thermal shrinkage, assuming a fictitious temperature change and coefficient of thermal expansion [33]. The linear shrinkage (δ) of the np-Au region was acquired for various times from the TXM images, as described in the results section. These radius shrinkages were used as the input for the fictitious thermal expansion coefficient (α) in the FEM, by setting $\alpha = \delta$. The corresponding stress caused by this linear shrinkage can therefore be obtained. The fictitious thermal expansion coefficient of the Ag–Au alloy remained zero, meaning no volume expansion/shrinkage happened. A fictitious temperature increase of 1 K was then applied to the model to induce the diameter expansion. The output fields were the von Mises stress and the in-plane strain, e_{11} and e_{22}, as a function of radial position within the wire.

Materials properties, including Young's modulus, Poisson ratio and yield stress are listed in Table 1. The elasto-plastic stress–strain curve of the Ag–25 Au alloy was constructed from the stress–strain curve of pure Ag [38], shifted to a higher yield stress to take into account the solid solution strengthening effect of Au. The relationship between the yield stress of pure Ag (σ_{Ag}) and the yield stress of a Ag–Au solid solution (σ_{Ag-Au}) was calculated using the following equation:

$$\sigma_{Ag-Au} = \sigma_{Ag} + kC^{1/2} \quad (1)$$

where $C = 0.25$ is the Au atom fraction in the Ag–Au alloy and $k = 6.36$ MPa at.%$^{-1/2}$ is a parameter which depends on C. The present value of k was determined from the relationship between the critical resolved shear stress of the Ag–Au alloy and C [37]. The resulting stress vs. plastic strain for Ag–25 Au is shown in Supplemental Fig. S.1. The values were used as an input for the FEM. The plasticity of np-Au is considered in the FEM, by inputting a relationship between the stress and the plastic strain, shown in Supplemental Fig. S.2. These values were calculated from the stress–strain curve of np-Au taken from the literature [39].

Table 1
Materials properties used in the FEM.

Property	Ag–25 Au	Ref.	np-Au	Ref.
Young's modulus (GPa)	82.2	[34]	7	[35]
Poisson ratio	0.39	[36]	0.20	[36]
Yield stress (MPa)	89.1	[37,38]	171	[39]

3. Results

3.1. Effect of alloy composition on dealloying behavior

3.1.1. In situ imaging of dealloying front

TXM images for five different alloys are shown in Fig. 3 for two typical dealloying times. Ag–40 Au achieved only a very shallow dealloying depth (~100 nm) before the dealloying front stopped. By contrast, Ag–35, 30, 25 and 20 Au showed a continuous dealloying with time, with no or very little diameter reduction and cracking except for Ag–20 Au, which showed a large reduction in diameter (up to 38%) and many cracks. Ag–25 Au also showed a much smaller diameter shrinkage, with the diameter changing from 16.3 μm to 16.1 μm in ~48 s, after the dealloying front had propagated 3.6 μm.

3.1.2. Dealloying kinetics

As described previously [40], the X-ray intensity profile along the radial direction of each individual image which corresponds to a specific dealloying time was averaged over a 2 μm width in the center of the TXM images (marked as a red rectangle in Fig. 3a). The derivative of the intensity was then calculated to determine the positions of the Ag–Au/np Au interface (dealloying front) and the acid/np-Au interface (sample surface) in the images. In Fig. 3e and f, the right side of the sample was outside the field of view and therefore the dealloying front could not be observed.

Fig. 4 shows the dealloying distance vs. time of four different Ag–Au alloy compositions, ranging from Ag-20, 25, 30 to 35 Au (the Ag–30 Au curve is taken from our previous work [27]). The velocities of the dealloying fronts propagating from both left and right sides of the samples were quantified. The average of these two values was plotted with an estimated error of 200 nm. This error was estimated based on both the limit of the instrument resolution and the finite exposure time, which result in slightly blurred dealloying fronts in the X-ray images. At very early dealloying stages, the exact position of the dealloying front cannot be accurately determined due to the phase effects from the sample surface.

Fig. 4 shows that, for all alloy compositions, the radial velocity of the dealloying front is constant with time, and that an increase in the Ag/Au ratio in the alloy leads to an increase in this dealloying front velocity. These constant rates were then extrapolated to dealloying time 0 s by linear fitting. The results of the linear fitting exhibit only a small deviation from the origin (<200 nm), which indicates that the dealloying front propagates with a constant velocity from the beginning of the dealloying process. For Ag–20 Au, the dealloying rate accelerated between 10 and 12 s, the last two points measured during dealloying: the front

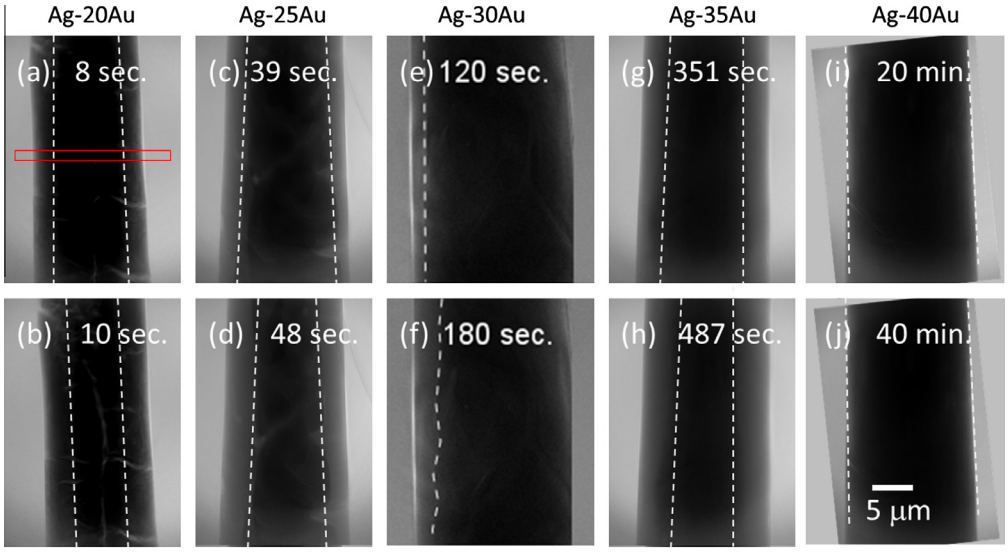

Fig. 3. TXM images of various Ag–Au alloys during dealloying with 10.9 M nitric acid: (a and b) Ag–20 Au, 8 and 10 s; (b and d) Ag–25 Au, 39 and 48 s; (e and f) Ag–30 Au, 120 and 180 s; (g and h) Ag–35 Au, 351 and 487 s; (i and j) Ag–40 Au, 20 and 40 min. Dotted lines indicate the position of the dealloying front as determined by the maximum in the differential of the intensity. The red rectangle indicates the central area where the dealloying front position was determined, as described in the later section. (For interpretation of the references to colour in this figure legend, the reader is referred to the web version of this article.)

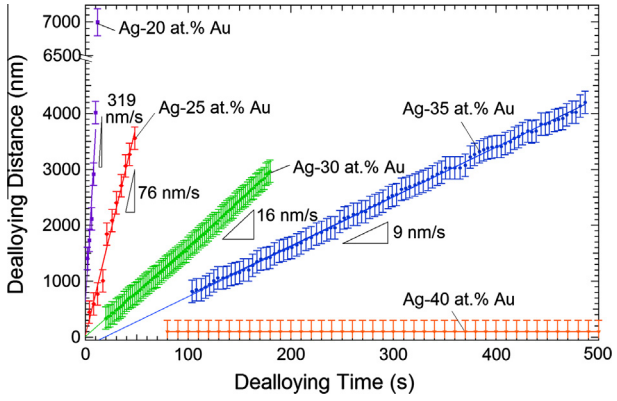

Fig. 4. The dealloying distance vs. dealloying time for different Ag–Au compositions with 10.9 M nitric acid (Ag–30 Au curve is from our previous work [27]).

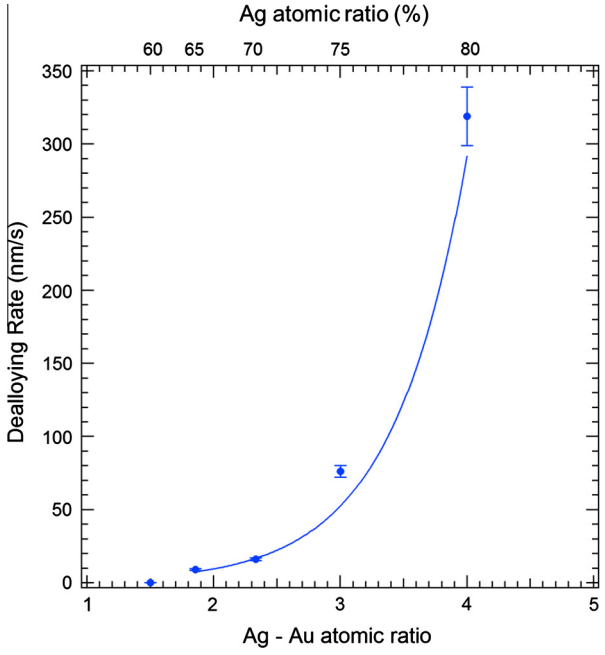

Fig. 5. Dealloying front velocity vs. Ag–Au atomic ratio with 10.9 M nitric acid.

velocity was 0.6 µm s^{-1} between 0 and 10 s but increased suddenly to 1.5 µm s^{-1}, between 10 and 12 s, which is the time interval where crack development is also observed. This acceleration is thus probably due to the short cuts provided to the acid by the cracks to the dealloying front, and the last data point (12 s) was not used in the linear fitting of Ag–20 Au. The relationship between the dealloying front velocity (v_d) and the Ag/Au atomic ratio ($R_{Ag–Au}$) is non-linear, as shown in Fig. 5, where the best fit ($R^2 = 0.99$) exponential equation is:

$$v_d = 0.3\exp(1.7R_{Ag–Au}) \quad (2)$$

The silver atomic concentration (C_{Ag}) is also shown in the figure for clarity. The physical meaning of using an exponential function and of the fitting parameters is discussed later.

Fig. 6 shows a series of *in situ* TXM images during the dealloying of Ag–20 Au. In addition to the dealloying front propagation, cracking and shrinkage were observed for this composition. A longitudinal crack at the center of the sample (marked with "A" on Fig. 6) initiated at 8 s. At 10 s, this crack propagated through the sample vertically by more than 32.5 µm, extending over the entire field of view. It then further widened at 12 s.

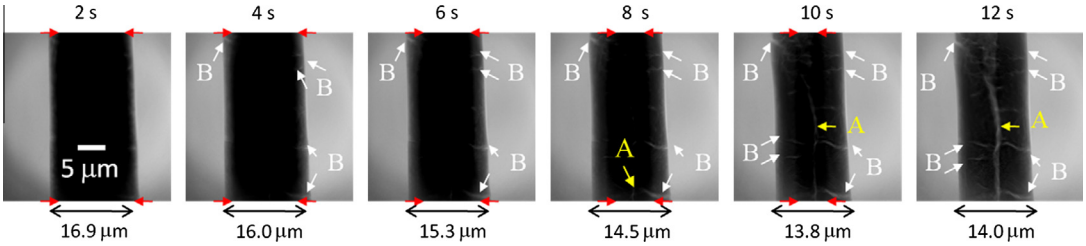

Fig. 6. TXM images of an *in situ* dealloying Ag–20 Au sample with 10.9 M nitric acid showing one longitudinal crack (A) and numerous radial cracks (a few are marked with B). Arrows (red) at the top and bottom of the images indicate the position of the dealloying front (for *in situ* dealloying videos, see Supplementary video S.1 online). (For interpretation of the references to colour in this figure legend, the reader is referred to the web version of this article.)

The projected crack width was measured to be 0.26, 0.53 and 1.24 μm after 8, 10 and 12 s, respectively. Numerous radial cracks (marked with "B" on Fig. 6) also formed. These radial cracks always extended to the depth of the dealloying front.

Fig. 7 is the top view and the side view of the crack in 3-D reconstruction of sample Ag–20 Au. The tomography data were taken after the sample had been dealloyed for ~30 s – well after the dealloying front had reached the sample center – and had been fully rinsed with deionized water. As shown in Fig. 7, a longitudinal crack (A) is nearly splitting the sample vertically. Also, numerous radial cracks (B) were observed.

The Ag–20 Au sample initial diameter of 17.8 ± 0.3 μm shrank to 14.0 ± 0.3 μm after full dealloying (12 s). Since the np-Au is the part of the sample that shrank during dealloying, the linear shrinkage of np-Au at a given time t can be calculated by as the ratio (δ) of change in sample diameter and the instantaneous width of the np-Au shell (taking the shrinkage which happened up to time t into account), as expressed in the following equation:

$$\delta(t) = \Delta D/d(t) + \Delta D \tag{3}$$

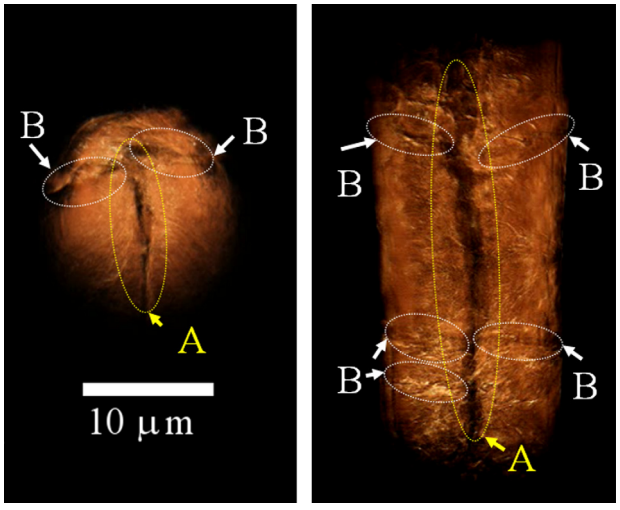

Fig. 7. 3-D tomographic reconstruction of the Ag-20 Au sample after being fully dealloyed with 10.9 M nitric acid (after 12 s dealloying) with top view (left) and side view (right) with one longitudinal crack (A) and numerous radial cracks (a few are marked with B) (for 3-D tomography reconstruction videos see Supplementary videos S.2–S.3 online).

where D is the sample diameter, ΔD is the change in diameter and $d(t)$ is the width of the np-Au shell at a given time t.

Fig. 8 shows D and δ as functions of dealloying time for Ag–20 Au. Here the material diameter D is calculated from the sample diameter D' minus the central crack (crack A) width. D is equivalent to the diameter of the Ag–Au alloy plus the np-Au. The difference between the sample diameter and the materials diameter is therefore the width of the

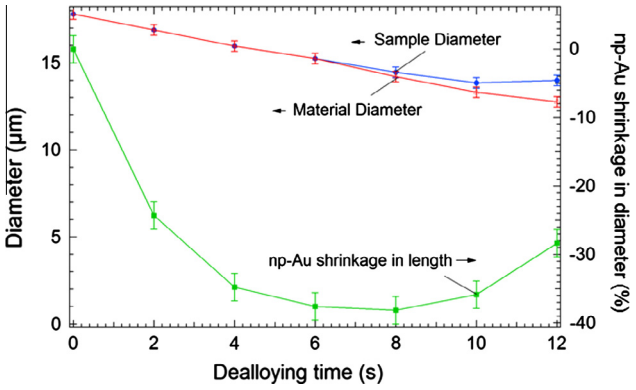

Fig. 8. Sample diameter (D), sample diameter shrinkage ($\Delta D/D$) and np-Au linear shrinkage (δ) vs. dealloying time, during dealloying of Ag–20 Au with 10.9 M nitric acid.

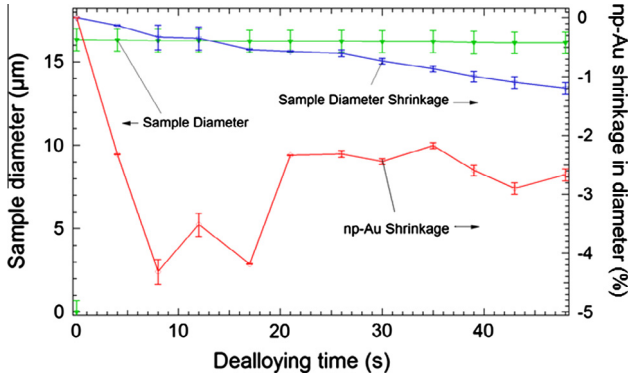

Fig. 9. Sample diameter (D), sample diameter shrinkage ($\Delta D/D$) and np-Au linear shrinkage (δ) vs. dealloying time, during dealloying of Ag–25 Au with 10.9 M nitric acid.

crack. It is apparent that the crack nucleated between 6 and 8 s and grew quickly between 10 and 12 s.

Fig. 9 shows D and δ as a function dealloying time in Ag–25 Au. The volume shrinkage is much less than in the Ag–20 Au system. The shrinkage of np-Au in length at 48 s was applied to the FEM to study the dealloying-induced stress and strain due to this volume shrinkage.

3.2. Effect of acid concentration on dealloying

The same imaging analysis method as described in the previous section was used to quantify the dealloying distance vs. dealloying time for different acid concentrations for Ag–30 Au samples, as shown in Fig. 10.

As for Fig. 10 where the acid concentration is constant but the Au alloy concentration varied, the dealloying front velocity is near constant up to the highest depth measured (3–5 μm); there is a clear increase in dealloying front velocity with increasing acid concentration, as summarized in Fig. 11. The error bars in concentration were calculated by assuming a 2% offset in volume when diluting the acid (2 ml error when preparing 100 ml solution), which results in a 0.3 M change.

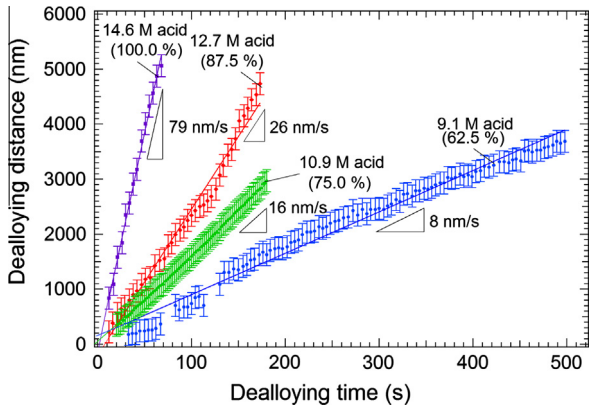

Fig. 10. Dealloying distance vs. dealloying time for Ag–30 Au dealloyed with different acid concentrations.

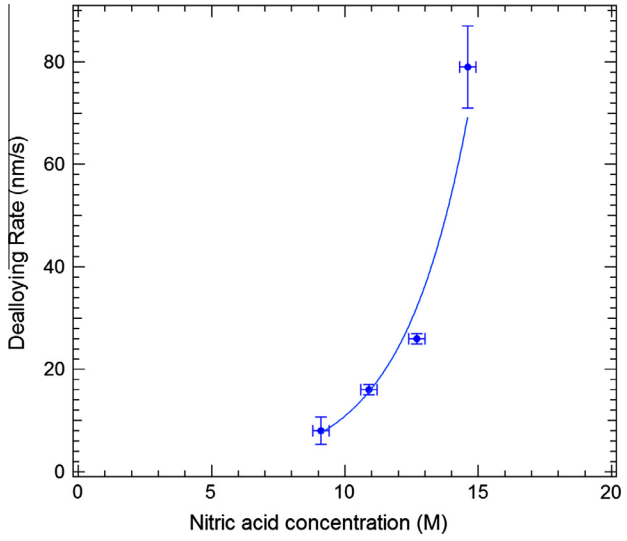

Fig. 11. Dealloying front velocity vs. nitric acid concentration for Ag–30 Au.

For the Ag–30 Au alloy, the dealloying front velocity (v_d, expressed in nm s^{-1}) depends exponentially on acid concentration (C_{HNO3}, expressed in M) according to:

$$v_d = 0.2\exp(0.40C_{HNO3}) \quad (4)$$

with $R^2 = 0.9759$. The physical meaning of using the exponential function and of the resulting fitting parameters is discussed later.

4. Discussion

4.1. Dealloying front velocity

The dealloying front velocity has been shown to be proportional to the current density or dissolution flux [27]. The dealloying front velocity measured here is a constant, which implies that the current density is also a constant, independent of the dealloying time. This indicates that the system has reached a steady-state current density. This further indicates that the free corrosion of Ag–Au with 20–35 Au and nitric acid of 7.3–14.6 M is well-above the E_c, as discussed in the literature [24,41], and thus a nanoporous structure forms.

Erlebacher proposed a model where the steady-state dissolution flux (J_{ss}) can be described as [20]:

$$J_{ss} = v_E\tau\exp[(e\phi - 9E_b/k_BT] \quad (5)$$

where v_E is the dissolution attempt frequency, τ is a constant ~ 1, E_b is the bond energy between the silver and gold in our case, e is the electron unit charge multiplied by the valence of a silver ion, which is unity, and ϕ is the over-potential. ϕ and E_b depend on the alloy composition and acid concentration and therefore $r_{Ag–Au}$ and C_{HNO3} determine the exponential terms as shown before, while v_E stays constant for a given temperature.

Another way that the alloy composition could affect the pore size and its evolution is due to a composition-dependent "pre-existing length scale" depending on the alloy composition [42]. Higher Ag composition, for instance, will reduce the mean diameter (ξ) of the Au percolation network but increase that of the Ag one, therefore providing a continuous path for dissolution of Ag without relying on the surface diffusion of Au.

Adapting one-dimensional percolation arguments, the relationship between ξ and the alloy composition can be written as [42]:

$$\xi = (1 + C_{Ag})a/(1 - C_{Ag}) \quad (6)$$

where C_{Ag} again is the Ag atomic concentration in the alloy and a is the nearest-neighbor spacing in the lattice. For the Ag–Au alloy, a is the lattice spacing of the (1 1 1) plane, d_{111}. The relationship between ξ and the dealloying front velocity can also be fitted with an exponential function ($R^2 = 0.9881$) giving:

$$v_d = 0.1477\exp(0.86\xi) \quad (7)$$

Therefore, provided the alloy composition is known, the dealloying velocity can be predicted.

4.2. FEM of the dealloying induced stresses and strains

The strain and stress states modeled for a partially dealloyed Ag–25 Au, computed at 9 s intervals between 12 and 48 s dealloying time, are presented in the following.

First, the strains measured from TXM images (δ) were used as the linear shrinkage of np-Au regions in the FEM as shown in Fig. 12 as the fictitious thermal expansion coefficients (α). Fig. 12 shows the radial strains e_{11} in the central plane (marked in Fig. 2) as a function of the radial distance for various dealloying times. The origin of the radial position is defined as the axis of symmetry of the cylinder as shown in Fig. 2. The np-Au shell exhibits a compressive radial strain (e_{11}), whose intensity increases from surface to the dealloying front. The maximum value at the front increases as the dealloying proceeds, from –4.3% (21 s) to –6.4% (48 s) while the minimum value at the surface decreases slightly from 0.0% (21 s) to 1.2% (48 s). The shrinkage of the np-Au shell results in a small amount of tensile strain in the Ag–25 Au. This strain remains almost constant in the Ag–Au core along the radial direction and increases as a function of dealloying time from ~0.002% (21 s) to 0.71% (48 s).

However, the magnitude of the radial strain presented in Fig. 12 is greater than the strains measured from the TXM images, δ. Because these simulated results do not reflect the experimental situation, modified α values, $\alpha = \delta/1.7$ were used to refine the FEM results. This factor 1.7 was determined from the ratio between the experimental averaged e_{11} and the averaged e_{11} from FEM using $\alpha = \delta$, both in the np-Au region. Fig. 13 shows the area-averaged radial strain of the np-Au shell vs. dealloying time with three different methods: (i) experimentally with strains calculated from TXM images (δ); (ii) numerically, with FEM using $\alpha = \delta$ and (iii) numerically, with $\alpha = \delta/1.7$. The latter case shows a much better match with the experimental results.

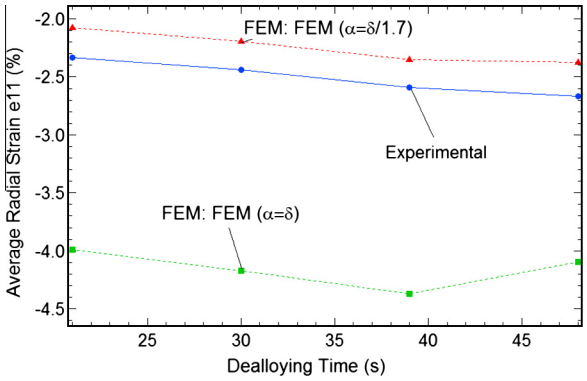

Fig. 13. The area-averaged radial strain of np-Au vs. **dealloying time during dealloying Ag–25 Au with 10.9 M nitric acid.** The strains were calculated from TXM images (δ), FEM using δ as α and FEM using $\delta/1.7$ as the α values.

Therefore, the following FEM results are all produced with $\alpha = \delta/1.7$. This discrepancy between α and δ needs to be further investigated.

Fig. 14 shows the radial strains e_{11} at the central location as a function of the radial distance at various times, using $\alpha = \delta/1.7$ in the FEM calculations. The trends remain similar to those shown in Fig. 14 but with the strain values matching the experimental result better. The maximum strain is at the dealloying front, which increases from –2.5% (21 s) to –3.2% (48 s) as the dealloying front proceeds, while the minimum value remains ~–2.0% (21–48 s).

Although only radial strain (shrinkage in diameter) could be observed experimentally in TXM images during dealloying of the cylindrical samples, it was assumed that unconstrained dealloying shrinkage was isotropic by replacing it with an isotropic thermal contraction in the FEM model. The model predicts a compressive longitudinal strain (e_{22}) that is independent of radial position in both the Ag–Au and np-Au regions, as shown in Fig. 15 at various dealloying times. The magnitude of e_{22} increases from –0.02% to –1.55% as dealloying proceeds from 21 to 48 s. The strain magnitude e_{22} in np-Au remains smaller than that of e_{11}. This can be explained by the fact that

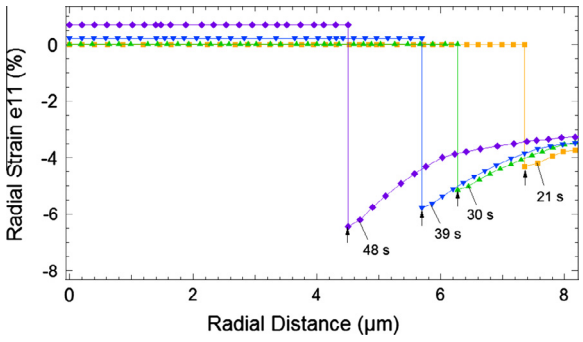

Fig. 12. Plot of dealloying induced radial strain (e_{11}) vs. radial distance after 21, 30, 39 and 48 s dealloying of Ag–25 Au with 10.9 M nitric acid as calculated by FEM using strains measured from TXM images (δ) as the α values.

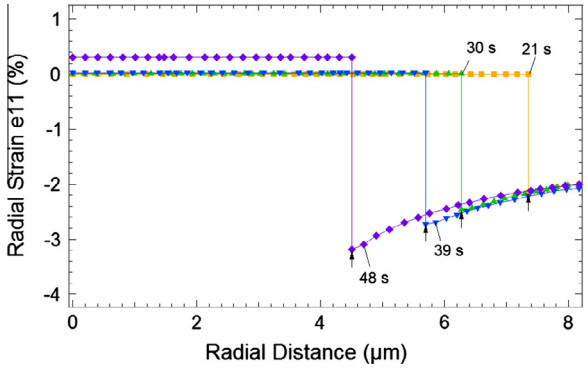

Fig. 14. Plot of dealloying induced radial strain (e_{11}) vs. radial distance at 21–48 s dealloying of Ag–25 Au with 10.9 M nitric acid as calculated by FEM using $\delta/1.7$ as the α values.

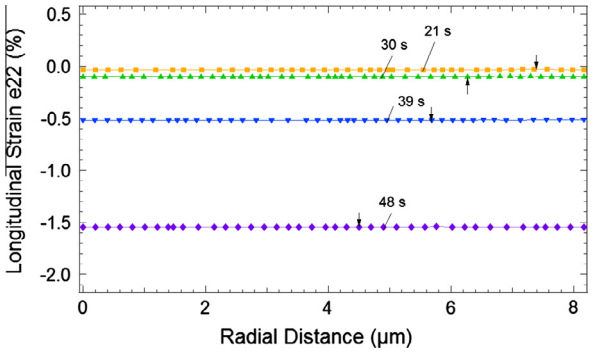

Fig. 15. Plot of dealloying induced longitudinal strain (e_{22}) vs. radial distance at 21–48 s dealloying of Ag–25 Au with 10.9 M nitric acid as calculated by FEM using $\delta/1.7$ as the α values.

the Ag–Au core is preventing the np-Au shell from shrinking longitudinally as much as it would if the two phases were not connected. While the dealloying front proceeds, more Ag–Au becomes np-Au and therefore the sample can increasingly shrink longitudinally.

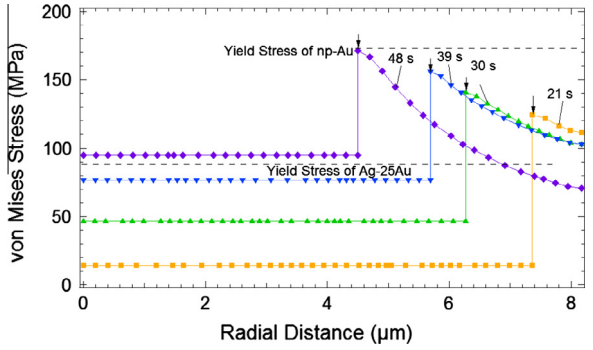

Fig. 16. Plot of the dealloying induced von Mises stress vs. radial distance to the axis of symmetry (center of the cylinder) at 21–48 s dealloying of Ag–25 Au with 10.9 M nitric acid as calculated by FEM ($\alpha = \delta/1.7$).

Fig. 16 shows the von Mises stress vs. radial distance at various dealloying times. The Ag–Au core is under a constant von Mises stress, which increases as a function of dealloying time. This stress eventually (48 s) exceeds the yield stress of Ag–25 Au (89.1 MPa, marked as dashed line in Fig. 16) and the Ag–Au core starts deforming plastically. In the np-Au shell, the stress never exceeds the yield stress (171 MPa). Near the dealloying front, the von Mises stress is as high as 170 MPa in the np-Au at 48 s dealloying. Along the radial direction, the stress decreases gradually. The np-Au is thus predicted to deform elastically up to this depth (4.2 μm) in Ag–25 Au. If the dealloying front proceeds deeper, plastic deformation is predicted to happen in the np-Au shell, especially near the dealloying front region where the stresses are highest.

To illustrate the edge effects, full maps of the von Mises stress, the radial strain e_{11} and the longitudinal strain e_{22}, as calculated by FEM, are shown in Fig. 17, Supplemental Figs. S.3 and S.4, respectively. At stress concentration regions, near the tip and the base, higher stresses and strains exist as compared to the rest of the sample but the difference is relatively minor.

In the future, the anisotropy of mechanical properties along different crystallographic orientations may be taken into account in the FEM. A close-form solution for the strain and stress components also needs to be discussed and compared to the FE calculations.

5. Conclusions

A high resolution transmission X-ray microscope was used to image the dealloying process of cylindrical Ag–Au alloys (16 μm in diameter) with various compositions (Ag-20 Au to Ag–40 Au, at.%) for various acid concentrations. A sharp front between the growing dealloyed np-Au shell and the shrinking Ag–Au alloy core propagates at a

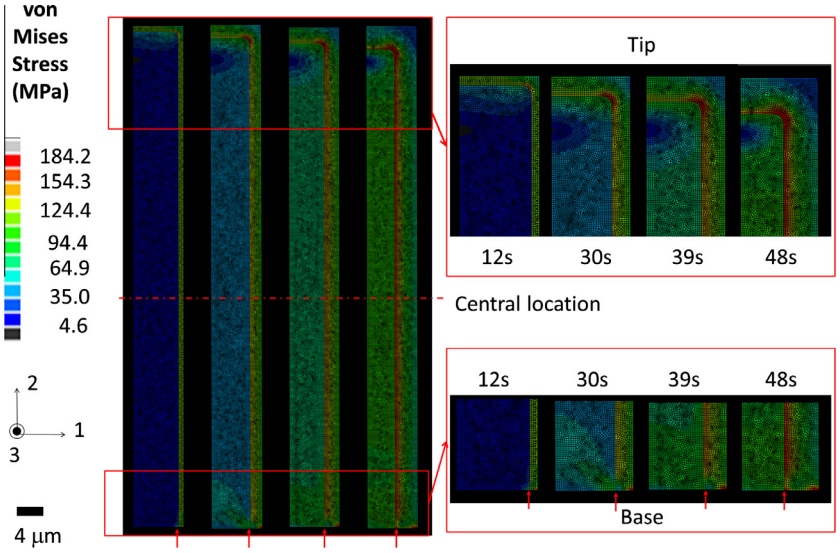

Fig. 17. The map of the von Mises stress as a function of dealloying time for Ag-25Au dealloyed with 10.9 M nitric acid, calculated by FEM ($\alpha = \delta/1.7$).

constant dealloying front velocity, v_d, except for the alloy with the highest Au concentration (40 at.% Au), for which dealloying stops after ~100 nm due to passivation. Only the alloy with the lowest Au concentration (20 at.% Au) developed cracks and sizeable diameter shrinkage (up to ~38%) during dealloying. The dealloying-induced stresses and strains were simulated with FEM for the Ag–25 Au system for 21–48 s of dealloying, which developed a small amount of shrinkage (compressive strain <3% for partial dealloying of 70% of sample volume). The FEM results show that compressive radial strains in the dealloyed shell of np-Au results in a tensile radial strain in the dense Ag–25 Au core. At 48 s of dealloying, the Ag–Au shell is under a von Mises stress which exceeds its yield stress and deforms plastically. For the np-Au shell, only the region near the dealloying front may exhibit a von Mises stress which exceeds its yield stress and therefore deforms plastically. For the region further away from the dealloying front, the np-Au deforms elastically.

For a constant 10.9 M acid concentration, the dealloying front velocity increases exponentially with the Ag/Au atomic ratio for alloys with 20–35 at.% Au. For a constant Ag–30 Au alloy composition, the dealloying front velocity scales exponentially with the acid concentration in the range 7.3–14.6 M. These exponential front velocity dependencies in both alloy composition and acid concentration can be explained by an existing model of steady-state dissolution flux. This flux exponentially relates to bond energy and over-potential, which both depend on alloy composition and acid concentration.

Acknowledgements

We gratefully thank Prof. Peter Voorhees (NU) for useful discussions throughout the experimental design and data analysis and Mr. Alex Deriy (APS) who helped with the *in situ* dealloying setup. X-ray imaging was assisted by Dr. Alix Deymier-Black (NU), Ms. Rachel Mak (NU) and Mr. Ashish Tripathi (U Melbourne). Use of the APS is supported by the US Department of Energy, Office of Science, Office of Basic Energy Sciences, under Contract No. DE-AC02-06CH11357.

Appendix A. Supplementary material

Supplementary data associated with this article can be found, in the online version, at http://dx.doi.org/10.1016/j.actamat.2013.05.039.

References

[1] Cox ME, Dunand DC. Mater Sci Eng A – Struct Mater Prop Microstruct Process 2011;528:2401–6.
[2] Erlebacher J, Seshadri R. MRS Bull 2009;34:6.
[3] Li HQ, Misra A, Baldwin JK, Picraux ST. Appl Phys Lett 2009:95.
[4] Gu XH, Xu LQ, Tian F, Ding Y. Nano Res 2009;2:386–93.
[5] Dixon MC, Daniel TA, Hieda M, Smilgies DM, Chan MHW, Allara DL. Langmuir 2007;23:2414–22.
[6] Qian LH, Shen W, Shen B, Qin GWW, Das B. Nanotechnology 2010;21:7.
[7] Wada T, Yubuta K, Inoue A, Kato H. Mater Lett 2011;65:1076–8.
[8] Zhang Q, Wang XG, Qi Z, Wang Y, Zhang ZH. Electrochim Acta 2009;54:6190–8.
[9] Tappan BC, Steiner SA, Luther EP. Angew Chem – Int Ed 2010;49:4544–65.
[10] Ding Y, Chen M. MRS Bull 2009;34:8.
[11] Qiu HJ, Xue LY, Ji GL, Zhou GP, Huang XR, Qu YB, et al. Biosens Bioelectron 2009;24:3014–8.
[12] Biener J, Wittstock A, Zepeda-Ruiz LA, Biener MM, Zielasek V, Kramer D, et al. Nat Mater 2009;8:47–51.
[13] Lang XY, Hirata A, Fujita T, Chen MW. Nat Nanotechnol 2011;6:232–6.
[14] Wittstock A, Zielasek V, Biener J, Friend CM, Baumer M. Science 2010;327:319–22.
[15] Xu C, Xu X, Su J, Ding Y. J Catal 2007;252:243–8.
[16] Qian LH, Yan XQ, Fujita T, Inoue A, Chen MW. Appl Phys Lett 2007;90:3.
[17] Yu Y, Gu L, Lang XY, Zhu CB, Fujita T, Chen MW, et al. Adv Mater 2011;23:2443.
[18] Kertis F, Snyder J, Govada L, Khurshid S, Chayen N, Erlebacher J. JOM – J Miner Metals Mater Soc 2010;62:50–6.
[19] Sieradzki K, Dimitrov N, Movrin D, McCall C, Vasiljevic N, Erlebacher J. J Electrochem Soc 2002;149:B370–7.
[20] Erlebacher J. J Electrochem Soc 2004;151:C614–26.
[21] Artymowicz DM, Erlebacher J, Newman RC. Philos Mag 2009;89:1663–93.
[22] Weissmuller J, Newman R, Jin H-J, Hodge A, Kysar J. MRS Bull 2009;34:10.
[23] Newman RC, Corcoran SG, Erlebacher J, Aziz MJ, Sieradzki K. MRS Bull 1999;24:24–8.
[24] Dursun A, Pugh DB, Corcoran SG. J Electrochem Soc 2005;152:B65–72.
[25] Qian LH, Chen MW. Appl Phys Lett 2007:91.
[26] Erlebacher J, Aziz MJ, Karma A, Dimitrov N, Sieradzki K. Nature 2001;410:450–3.
[27] Chen Y-cK, Wang S, Lee W-K, McNulty I, Voorhees PW, Dunand DC. Acta Mater 2013;61:1118–25.
[28] Donald IW, Metcalfe BL. J Mater Sci 1996;31:1139–49.
[29] Chen Y, Lo T, Chu Y, Yi J, Liu C, Wang J, et al. Nanotechnology 2008;19. 395302-1-5.
[30] Chu YS, Yi JM, De Carlo F, Shen Q, Lee WK, Wu HJ, et al. Appl Phys Lett 2008:92.
[31] Natterer F. The mathematics of computerized tomography. New York: Wiley; 1986.
[32] Murray NGD, Dunand DC. Acta Mater 2004;52:2279–91.
[33] Zwigl P, Dunand DC. Mater Sci Eng A – Struct Mater Prop Microstruct Process 2002;335:128–36.
[34] Kaye GWC, Laby TH. Tables of physical and chemical constants. 15th ed. London: Longman; 1993.
[35] Parida S, Kramer D, Volkert C, Rosner H, Erlebacher J, Weissmuller J. Phys Rev Lett 2006:97.
[36] Mathur A, Erlebacher J. Appl Phys Lett 2007:90.
[37] Svitak JJ, Asimow RM. Trans Metall Soc AIME 1969;245:209.
[38] Kovacs I, Voros G. Int J Plast 1996;12:35–43.
[39] Biener J, Hodge AM, Hayes JR, Volkert CA, Zepeda-Ruiz LA, Hamza AV, et al. Nano Lett 2006;6:2379–82.
[40] Chen YCK, Chu YS, Yi J, McNulty I, Shen Q, Voorhees PW, et al. Appl Phys Lett 2010:96.
[41] Dursun A, Pugh DV, Corcoran SG. Electrochem Solid State Lett 2003;6:B32–4.
[42] Rugolo J, Erlebacher J, Sieradzki K. Nat Mater 2006;5:946–9.